



## RESEARCH LETTER

10.1002/2017GL072940

## Special Section:

Early Results: Juno at Jupiter

## Key Points:

- JIRAM data from first Juno orbit highlighted the presence of several ovals in Jupiter's southern hemisphere
- Column densities and altitudes for an NH<sub>3</sub> cloud and an N<sub>2</sub>H<sub>4</sub> haze have been retrieved for three ovals in the region between 60–120°W and 30–45°S
- Evidences of cyclonic and anticyclonic structures inside the ovals have been found

## Correspondence to:

G. Sindoni,  
giuseppe.sindoni@iaps.inaf.it

## Citation:

Sindoni, G., et al. (2017), Characterization of the white ovals on Jupiter's southern hemisphere using the first data by the Juno/JIRAM instrument, *Geophys. Res. Lett.*, 44, doi:10.1002/2017GL072940.

Received 7 FEB 2017  
Accepted 31 MAR 2017

## Characterization of the white ovals on Jupiter's southern hemisphere using the first data by the Juno/JIRAM instrument

G. Sindoni<sup>1</sup> , D. Grassi<sup>1</sup> , A. Adriani<sup>1</sup> , A. Mura<sup>1</sup> , M. L. Moriconi<sup>1,2</sup> , B. M. Dinelli<sup>2</sup> , G. Filacchione<sup>1</sup> , F. Tosi<sup>1</sup> , G. Piccioni<sup>1</sup> , A. Migliorini<sup>1</sup> , F. Altieri<sup>1</sup> , F. Fabiano<sup>2,3</sup> , D. Turrini<sup>1,4</sup> , R. Noschese<sup>1</sup> , A. Cicchetti<sup>1</sup> , S. Stefani<sup>1</sup> , S. J. Bolton<sup>5</sup> , J. E. P. Connerney<sup>6</sup> , S. K. Atreya<sup>7</sup> , F. Bagenal<sup>8</sup> , C. Hansen<sup>9</sup> , A. Ingersoll<sup>10</sup> , M. Janssen<sup>11</sup> , S. M. Levin<sup>11</sup> , J. I. Lunine<sup>12</sup> , G. Orton<sup>11</sup> , A. Olivieri<sup>13</sup>, and M. Amoroso<sup>13</sup>

<sup>1</sup>INAF-Istituto di Astrofisica e Planetologia Spaziali, Rome, Italy, <sup>2</sup>CNR-Istituto di Scienze dell'Atmosfera e del Clima, Bologna, Italy, <sup>3</sup>Dipartimento di Fisica e Astronomia, Università di Bologna, Bologna, Italy, <sup>4</sup>Departamento de Física, Universidad de Atacama, Copiapó, Chile, <sup>5</sup>Space Science and Engineering Division, Southwest Research Institute, San Antonio, Texas, USA, <sup>6</sup>NASA Goddard Space Flight Center, Greenbelt, Maryland, USA, <sup>7</sup>Planetary Science Laboratory, University of Michigan, Ann Arbor, Michigan, USA, <sup>8</sup>Laboratory for Atmospheric and Space Physics, University of Colorado Boulder, Boulder, Colorado, USA, <sup>9</sup>Planetary Science Institute, Tucson, Arizona, USA, <sup>10</sup>Geological and Planetary Sciences, California Institute of Technology, California, USA, <sup>11</sup>NASA, Jet Propulsion Laboratory, California, USA, <sup>12</sup>Department of Astronomy, Cornell Center for Astrophysics and Planetary Science, Cornell University, New York, USA, <sup>13</sup>Agenzia Spaziale Italiana, Rome, Italy

**Abstract** During the first perijove passage of the Juno mission, the Jovian InfraRed Auroral Mapper (JIRAM) observed a line of closely spaced oval features in Jupiter's southern hemisphere, between 30°S and 45°S. In this work, we focused on the longitudinal region covering the three ovals having higher contrast at 5 μm, i.e., between 120°W and 60°W in System III coordinates. We used the JIRAM's full spectral capability in the range 2.4–3 μm together with a Bayesian data inversion approach to retrieve maps of column densities and altitudes for an NH<sub>3</sub> cloud and an N<sub>2</sub>H<sub>4</sub> haze. The deep (under the saturation level) volume mixing ratio and the relative humidity for gaseous ammonia were also retrieved. Our results suggest different vortex activity for the three ovals. Updraft and downdraft together with considerations about the ammonia condensation could explain our maps providing evidences of cyclonic and anticyclonic structures.

### 1. Introduction

The white ovals, together with the Great Red Spot (GRS), are the most prominent features in Jupiter's atmosphere. They were first observed by ground-based measurements [Peek, 1958] then, in more detail during the flybys of Jupiter, carried out by the NASA Voyager probes in 1979 and during the extensive in-system tour performed by the NASA Galileo spacecraft in 1995–2003. These ovals are in a stable configuration known as a “Karman vortex street,” where anticyclones are staggered with cyclones [Youssef and Marcus, 2003]. These vortices appear very bright in the visible range and, for this reason, they are usually called “white.” Their visible brightness is due to the scattering of the sunlight by upper clouds and hazes condensed there. On the other hand, they appear very dark in the spectral range where the thermal radiation becomes dominant since thick clouds block photons coming from the deeper and hotter atmospheric layers. Color changes in the visible range, from white to red, have been observed in ovals [Go et al., 2006]. The reddish color is usually attributed to red “chromophores” [West et al., 1986], which are products of a series of complex chemical reactions, such as the UV photolization of ammonia with acetylene [Carlson et al., 2016]. These chromophores can act as coating material for the ammonia particles.

The current understanding of the cloud structure in the Jupiter's atmosphere is mainly related to theoretical models based on the thermochemical equilibrium theory [Weidenschilling and Lewis, 1973; Atreya et al., 1999]. They expect an ammonia ice layer at about 700 mbar, an ammonium hydrosulfide cloud layer at about 2 bars, and a water cloud layer with a base near 6 bars. Moreover, observations from the ground and from space in the visible, near, and thermal infrared provided important information about the aerosol composition of the planet [West et al., 1986, 2004]. In particular, the equatorial region, the GRS, and other small-scale cloud formations (as the ovals) were investigated by using the Galileo/SSI (Solid-State Imaging) instrument by

*Banfield et al.* [1998]. They modeled the atmosphere with a stratospheric haze layer, a denser upper tropospheric haze, and a cloud-like layer at pressures between 600 and 950 mbar. Their results suggested an increase of the altitude and of the aerosol optical depth inside the GRS and the white ovals with a two-cell structure with subsidence in the upper troposphere and upwelling in the lower troposphere. The three-layered structure for the cloudy atmosphere of Jupiter was also confirmed by *Irwin et al.* [1998]. Their analysis of Galileo/NIMS (Near-Infrared Mapping Spectrometer) spectra suggested the presence of a tropospheric haze at 200 mbar, an ammonia cloud at about 700 mbar, and an ammonium hydrosulfide cloud at pressures between 1.4 and 5 bars. Using the Galileo/NIMS and SSI data, *Dyudina et al.* [2001] investigated the cloud structure over the GRS and a white oval. They again suggested an increase in the optical thickness and in the elevation of the cloud inside both the atmospheric structures. Radiative transfer modeling of the infrared spectra in the 1–2  $\mu\text{m}$  range acquired by using ground-based measurements with Keck telescope [*de Pater et al.*, 2010] showed an overall similar vertical structure of all the studied features (GRS, Oval BA, and two white ovals at 41°S). An atmospheric model based on three layer hazes (2–200 mbar, 200–650 mbar, and 650–700 mbar) composed of ammonia ice particles revealed that the particle densities of the tropospheric-stratospheric hazes in the two white ovals are about 5–8 times smaller than in the GRS and Oval BA. The center of the vortexes shows a cloud at a pressure below of 600 mbar [*Dyudina et al.*, 2001], which is approximately the ammonia condensation level considering the expected mixing ratio in Jupiter's atmosphere. An optically thick cloud near the  $\text{NH}_3$  condensation level should contain large  $\text{NH}_3$ -ice particles, which drop down to the equilibrium condensation level where they sublime [*West et al.*, 1986]. Thus, gaseous  $\text{NH}_3$  depletion is associated with cloud formation. Both large-scale updrafts and turbulence can bring  $\text{NH}_3$  back into the cloud raising in altitude its upper boundary.

Simultaneous observations in the solar (below  $\sim 2 \mu\text{m}$ ) and thermal ( $\sim 5 \mu\text{m}$ ) spectral ranges highlighted the presence of hot rings (225–250 K) surrounding the periphery of ovals [*de Pater et al.*, 2010]. Since these thermal bright regions should be cloud-free down to about 5 bars, they suggested that anticyclones could extend vertically from the water cloud to the tropopause. Moreover, the observation of an anticorrelation in the opacities of the high tropospheric haze and of the low  $5 \mu\text{m}$  absorbing cloud could be explained by the descent of air at high altitude and the air ascent at low altitude, and vice versa [*Dyudina et al.*, 2001].

The cloud structure of the Jupiter's atmosphere, and in particular the nature of vortex features, as the GRS and the white ovals, is still puzzling. Indeed, only a very limited number of ovals has been investigated in detail by using the visible and infrared spectroscopy. Space-borne new instruments will cast light on this issue, thanks to their improved spatial resolution and the possibility to have a relatively long-time monitoring of the atmosphere.

Here we report the preliminary results about the cloud and haze structures inside and outside three ovals in the southern hemisphere of Jupiter obtained by the analysis of the Jovian InfraRed Auroral Mapper (JIRAM) observations acquired during the first perijove passage of the NASA spacecraft Juno after orbit insertion (PJ1). Spectral observations with a typical spatial resolution of around 250 km at the 1 bar level, the highest achieved so far from spacecraft, allow for an accurate characterization of these peculiar atmospheric features.

## 2. Data Set

The JIRAM instrument, aboard the NASA/Juno spacecraft, is composed of an infrared imager (IMG) and a spectrometer (SPE) [*Adriani et al.*, 2014], sharing a common optical head. The imager is further split in two spectral channels: L-filter, centered at  $3.45 \mu\text{m}$  with a 290 nm bandwidth, and M-filter, centered at  $4.78 \mu\text{m}$  with a 480 nm bandwidth. Each channel has a field of view (FOV) of  $1.75^\circ \times 5.94^\circ$  ( $128 \times 432$  pixels corresponding to the along- and across-track directions) and an instantaneous field of view (IFOV) of about  $250 \times 250 \mu\text{rad}$ . The spectrometer, based on grating diffraction of a pixel size slit, covers the spectral interval 2.0–5.0  $\mu\text{m}$  with a spectral resolution around 12 nm and has a FOV of  $3.52^\circ$  (across track) sampled by 256 pixels with a square IFOV of  $250 \times 250 \mu\text{rad}$ . The radiometric calibration is described in *Adriani et al.* [2014], whereas in-flight performances were first evaluated during the Earth-Moon flyby that occurred in October 2013 [*Adriani et al.*, 2016]. In this work we used the M-filter of the IMG for the context and the SPE for the characterization analysis.

Juno orbit insertion successfully occurred on 4 July 2016, and during its first perijove passage (27–28 August 2016), JIRAM acquired measurements covering almost the entire planet. In particular, JIRAM highlighted the presence of the white oval belt in the southern hemisphere, between 30°S and 45°S. In this work, we focused

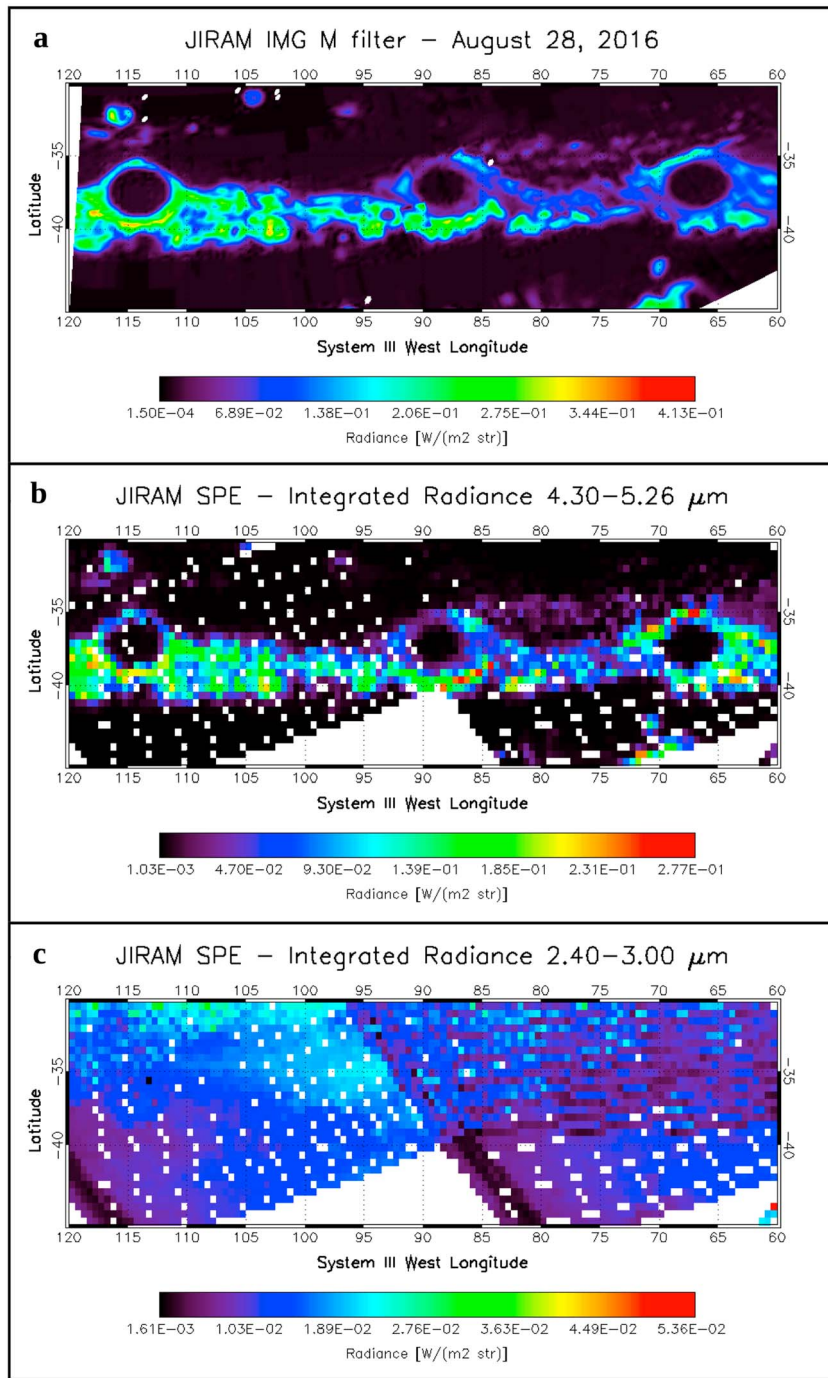


**Figure 1.** (a) M-filter single image acquired by JIRAM imager on 28 August 2016, where the three main ovals are clearly visible in the southern hemisphere of Jupiter. Integrated radiance in the (b) 4.30–5.26 μm and (c) 2.40–3.00 μm spectral ranges as acquired by the JIRAM spectrometer during the first orbit. In Figures 1b and 1c spectra are averaged in square bins of size 0.5° in planetocentric longitude and latitude. Data are projected in System III West coordinates, and the blank bins represent no coverage.

on the longitudinal region covering the three ovals having higher contrast at 5 μm, i.e., between 60°W and 120°W (in System III coordinates, Figure 1). Hereafter we refer to the region in this planetocentric rectangle as our region of interest (ROI). The identified ovals are all centered at a latitude of about 37°S and at longitudes of about 115°W, 88°W, and 67°W for Oval#1, Oval#2, and Oval#3, respectively. In the M band

they show approximately the same diameter of less than  $5^\circ$  on both axes. At that latitude, this angular diameter results in a size of about  $5000 \times 6000$  km.

In order to achieve the best spatial coverage, we divided the ROI in 3600 square bins of  $0.5^\circ$  in both latitude and longitude. The JIRAM spectrometer dayside acquisitions in PJ1 covered about 85% of these bins with a variable number of spectra spanning from 1 to 19, with an average of about 3. Since the variability in the observational (incidence, emission, and phase) angles of spectra falling into each bin is mostly of the order of few degrees or less, measurements were then averaged to build a data set composed of 3068 mean spectra (Figures 1b and 1c).

We estimated the instrumental noise affecting the measurements by the standard deviation of a selected set of 522 spectra acquired when the JIRAM instrument pointed to deep space in the same science session. Therefore, our data set has a mean signal-to-noise ratio of 632 with a maximum of 1703, a minimum of 6, and a standard deviation of 269 at  $2.75 \mu\text{m}$ .

### 3. The Analysis Procedure

#### 3.1. Method

Clouds and hazes strongly affect the JIRAM spectra. We limited our analysis to the spectral range between  $2.4$  and  $3 \mu\text{m}$  since it is sensitive to reflected sunlight and it can be used to sound the higher troposphere and the stratosphere. Moreover, it appears to be free from any calibration or instrumental issue. This range covers the spectral features of both gasses and particles of Jupiter's atmosphere and, for this reason, their interaction with radiation should be appropriately treated by using multiple scattering radiative transfer techniques.

The retrieval of the atmospheric composition exploits a data inversion technique with the Bayesian approach [Rodgers, 2000]. It uses the Gauss-Newton iterative procedure to minimize the  $\chi^2$  function. The solution at the  $n$ th iterative step is

$$x_{n+1} = x_n + (S_a^{-1} + K_n^T S_e^{-1} K_n)^{-1} (K_n^T S_e^{-1} [y - F(x_n)] - S_a^{-1} [x_n - x_a]) \quad (1)$$

where  $x$  is the state vector of the free parameters,  $y$  is the vector with the measured radiances,  $F$  is the simulated spectrum,  $K$  is the Jacobian matrix,  $x_a$  is the a priori knowledge of the state vector, and  $S_a$  and  $S_e$  are the variance-covariance matrices for  $x_a$  and  $y$ , respectively. The synthetic spectrum  $F$  takes into account the multiple scatterings, both by molecules and particles, and it is computed by using a line-by-line code in plane-parallel approximation [Ignatiev *et al.*, 2005]. This approach is suitable for simulating nadir or slant observations (incidence and emission angles  $< 70^\circ$ ), as is our case. Finally, the convergence criterion takes into account the  $\chi^2$  minimization. Convergence is reached when the minimum  $\chi^2$  does not decrease within 10 subsequent iterations.

#### 3.2. Atmospheric Model

The a priori knowledge of Jupiter's atmosphere is based on the model suggested by Grassi *et al.* [2010] and takes into account the gaseous opacities by  $\text{CH}_4$ ,  $\text{H}_2\text{O}$ ,  $\text{NH}_3$ , and  $\text{PH}_3$  and the collision-induced absorptions by  $\text{H}_2\text{-H}_2$ ,  $\text{H}_2\text{-He}$ , and  $\text{H}_2\text{-CH}_4$ . We used a temperature-pressure profile for Jupiter's atmosphere as derived from the Galileo Probe data [Seiff *et al.*, 1998], which can be considered representative also for the conditions in ovals [de Pater *et al.*, 2010]. Two tropospheric clouds and a stratospheric haze describe the atmospheric particulate component. The properties of the deepest  $\text{NH}_4\text{SH}$  cloud we considered are the ones suggested by Giles *et al.* [2015]. They are assumed to have single scattering albedo  $\omega = 0.9$  and asymmetry factor  $g = 0.7$  for the Henyey-Greenstein phase function in the entire spectral range of our interest. Moreover, the  $\text{NH}_4\text{SH}$  cloud is considered to extend between 1.3 and 0.73 bars with a constant volume density of  $2.16 \text{ particle/cm}^3$ . Methane photochemistry models produced a haze of complex hydrocarbons in the stratosphere of Jupiter that was postulated to coat the ammonia clouds below [Atreya *et al.*, 2005], thus obscuring them except for fresh clouds that alone could be spectrally identified [Baines *et al.*, 2002]. Laboratory experiments [Kalogerakis *et al.*, 2008] suggested tholin as a possible coating substance for  $\text{NH}_3$  ice particles. In our work, we computed the single scattering parameters for the tholin-coated  $\text{NH}_3$  cloud by using the BART code [Quirantes and Delgado, 1997], which is based on the Aden-Kerker theory, starting from the refractive index by Howett *et al.* [2007] and Khare *et al.* [1984] for ammonia ice and tholin, respectively. We tested different

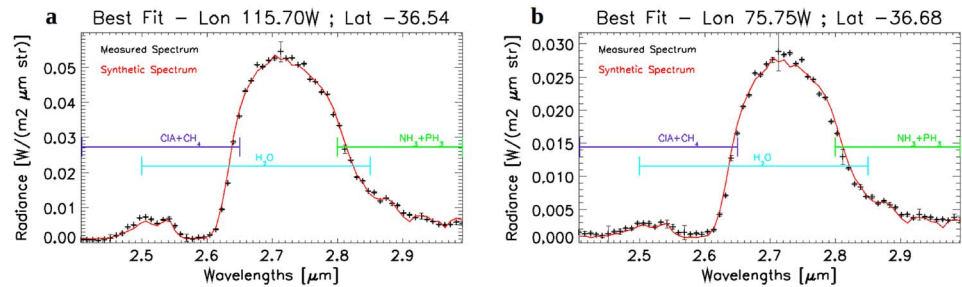


**Figure 2.** Example of two spectral best fits as a result of the data inversion procedure. The black dots and the red line represent the JIRAM measured mean spectrum and the best fit synthetic spectrum, respectively. The spectra refer to a bin inside the Oval#1 around (a) longitude 115.70°W and latitude 36.54°S and a bin outside the ovals around (b) longitude 75.75°W and latitude 36.68°S. The horizontal colored bars highlight the ranges where the gaseous features affect the spectrum.

tholin refractive indexes covering the spectral region of interest as suggested in the work by *Brassé et al.* [2015]. The ones from *Khare et al.* [1984] provided the best fit results on a sample of our data set. For this cloud we assumed a Gaussian vertical distribution between 1 bar and 200 mbar with the center at 500 mbar and a volume density of about 19 particle/cm<sup>3</sup>. Finally, we considered a hydrazine (N<sub>2</sub>H<sub>4</sub>) stratospheric haze as suggested by *Moreno* [1996] with a Gaussian vertical distribution between 40 and 20 mbar centered at 30 mbar and a particle volume density of about 4 particle/cm<sup>3</sup>. The optical properties for the haze were computed by using the refractive index by *Clapp and Miller* [1996] with a code based on the Mie theory. Finally, the solar spectrum was modeled following *Drummond and Thekaekara* [1973] and rescaled according to the actual heliocentric distance at the time of the acquisition.

The analysis procedure retrieves for each bin, starting from the reported a priori values (apv), the following parameters: 1) the column number density for the NH<sub>3</sub>-tholin cloud (NH<sub>3</sub>-Tho\_cnd): apv =  $2.8 \times 10^7$  #/cm<sup>2</sup>; 2) the peak altitude of the NH<sub>3</sub>-tholin cloud (NH<sub>3</sub>-Tho\_alt): apv = 17.45 km; 3) the column number density for the N<sub>2</sub>H<sub>4</sub> haze (N<sub>2</sub>H<sub>4</sub>\_cnd): apv =  $2.0 \times 10^6$  #/cm<sup>2</sup>; 4) the peak altitude of the N<sub>2</sub>H<sub>4</sub> haze (N<sub>2</sub>H<sub>4</sub>\_alt): apv = 70.10 km; 5) the deep mixing ratio of gaseous ammonia (NH<sub>3</sub>\_vmr\_deep): apv =  $6.77 \times 10^{-4}$ ; and 6) the relative “humidity” of gaseous ammonia (NH<sub>3</sub>\_rh): apv = 2.02%.

We fixed the radii ratio to 0.5 and the total radius to 0.8 μm for the tholin-coated NH<sub>3</sub> particles and the radius of the N<sub>2</sub>H<sub>4</sub> haze to 0.3 μm as the best result of several tests obtained from a sample of our data set. Among the gaseous atmospheric components, only ammonia showed variability in the analyzed spectral range. The other atmospheric quantities were fixed to their a priori values. A typical example of spectral best fit is displayed in Figure 2.

The quality of the retrieval is assessed by using the  $\chi^2$ . Results showing a reduced  $\chi^2$  greater than 50 are discarded. Then, for each parameter, we further filtered the retrieved values, discarding those out of the 99.9% confidence level for the statistical distribution of the parameter population on the entire retrieved data set. This statistical filter, in fact, rules out retrieved values with a high probability to be nonphysical, even though providing a good fit (low  $\chi^2$ ). Following this approach, we finally discarded about 16.5% of our results and retained retrievals obtained at around 2560 out of 3068 bins.

### 3.3. Uncertainties

We estimated the uncertainties for the retrieved parameters by applying the retrieval procedure to a simulated synthetic data set. The statistics on our retrieved data set naturally provide the range of variability of the considered parameters. We created a set of 100 synthetic spectra for each of the six parameters with randomly variable values in that range, obtaining a total of 600 synthetic spectra. After the addition of the instrumental noise, we analyzed them. The mean differences between the known random parameters used for the spectra generation and the retrieved parameters provide the uncertainties on each of them. Thus, we obtained 24.76%, 29.77%, 69.59%, 63.36%, 49.23%, and 32.05% for the relative maxima uncertainties on NH<sub>3</sub>-Tho\_cnd, NH<sub>3</sub>-Tho\_alt, N<sub>2</sub>H<sub>4</sub>\_cnd, N<sub>2</sub>H<sub>4</sub>\_alt, NH<sub>3</sub>\_vmr\_deep, and NH<sub>3</sub>\_rh, respectively, over our data set. The two parameters related to the upper haze are those with higher uncertainty, whereas the retrieval of other parameters has errors of about 30%.



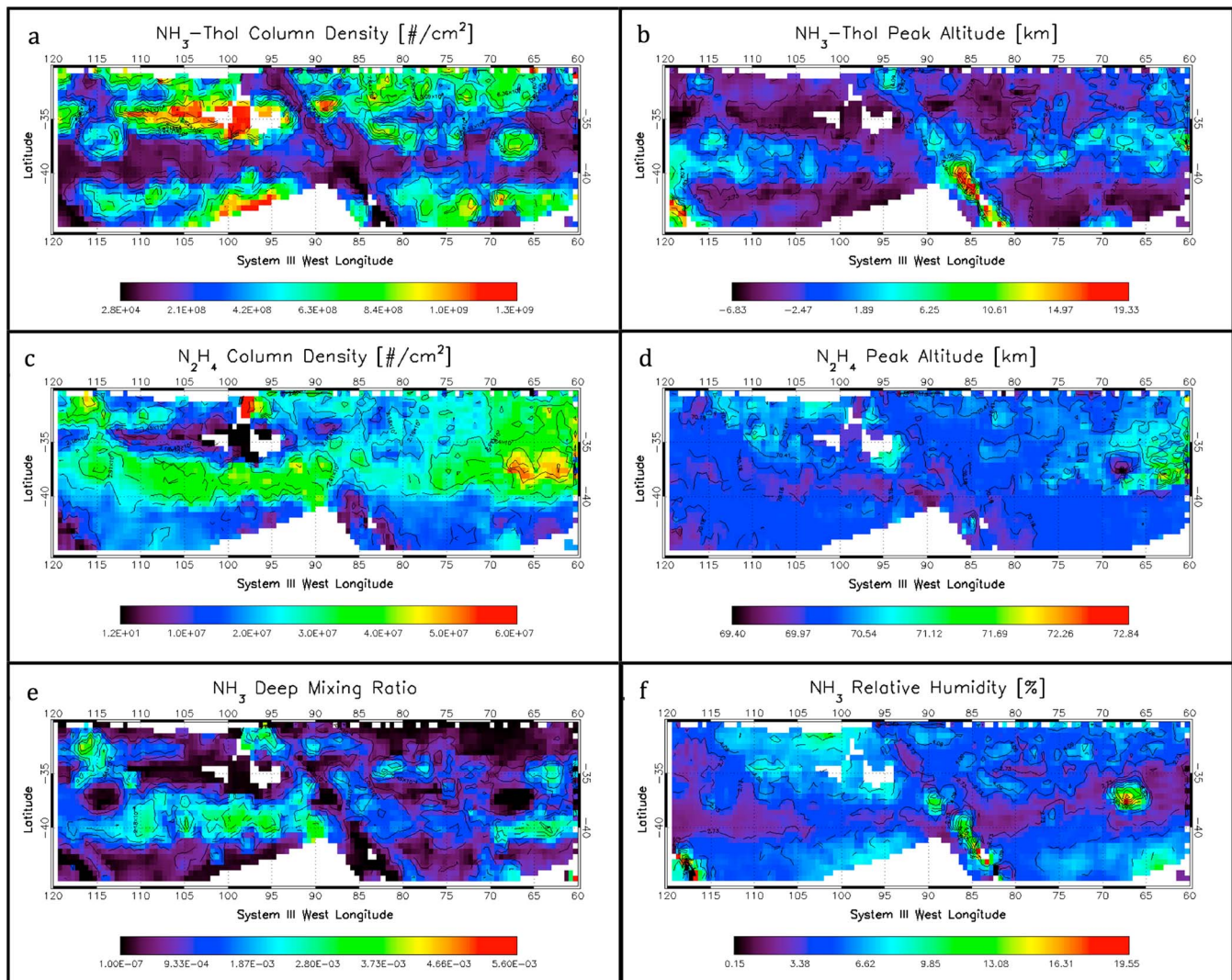


**Figure 3.** Maps of the retrieved parameters over the ovals ROI. Blank data represents no coverage or discarded results. (top row, left) Column densities and (right) peak altitudes for the  $\text{NH}_3$ -tholin clouds. (middle row, left) Column densities and (right) peak altitudes for the  $\text{N}_2\text{H}_4$  haze. (bottom row, left) Deep volume mixing ratio and (right) relative humidity for the gaseous ammonia. Column densities and altitudes are expressed in particle/ $\text{cm}^2$  and km above the 1 bar level, respectively, whereas other quantities are dimensionless.

#### 4. Results and Discussion

In Figure 3 we report the main results of the analysis of JIRAM's spectroscopic data in the ROI. Maps of retrieved parameters are smoothed over two neighboring points to improve legibility.

The entire latitudinal belt between  $41^\circ$  and  $37^\circ\text{S}$  is characterized, for the most part, by very low  $\text{NH}_3$ -tholin cloud densities at altitudes relatively higher than the surrounding atmosphere. The three ovals are generally identifiable in all the retrieved maps. However, Oval#1 and Oval#3 show more prominent features. They are mainly characterized by higher column densities for the  $\text{NH}_3$ -tholin cloud. The first cloud (Figure 3, top row) has values around  $8.0 \times 10^8$  particle/ $\text{cm}^2$  in Oval#1 and Oval#3, whereas Oval#2 shows lower values by a factor of 2. In Oval#2 and Oval#3, the thickness of their  $\text{NH}_3$ -tholin cloud increases from the border to the center of the vortex. On the contrary, the cloud thickness at the center of Oval#1 is 1.5 times lower than in the surrounding ring, which delimits the boundary of the vortex. In all the ovals we find an increasing altitude (measured from the pressure level of 1 bar) of the cloud from the boundary rings, with a peak at about  $-1$  km (1.04 bar), toward the vortex center, where the peak is at about 10 km (660 mbar). This result is in agreement with previous observations by Galileo/NIMS and Galileo/SSI data [Dyudina et al., 2001], where

the altitude of the  $\text{NH}_3$  ice cloud in the center of a white oval is at pressures less than 600 mbar. These instruments also observed an increase of the cloud thickness from the boundary ring toward the center of the vortex. Our analysis shows a similar behavior for Oval#3 and partially for Oval#2, whereas Oval#1 exhibits the opposite configuration. A possible explanation for these differences can be found in the updrafts and downdrafts in the centers of vortices that carry gaseous ammonia and condensed particles [West *et al.*, 1986]. In Oval#2 and Oval#3 an updraft transports the  $\text{NH}_3$  gas to higher altitudes (above 10 km, 660 mbar), where it condenses into ice particles. Then they subside in the ring boundary and sublimate at lower altitude. This is consistent with the behavior of an anticyclonic structure in a giant planet [Irwin, 2009; de Pater *et al.*, 2011]. On the contrary, in Oval#1,  $\text{NH}_3$  condenses at lower altitudes (around 940 mbar) in the ring and then ice particles move with increasing altitudes (up to the level around 660 mbar) toward the center, where they subside. The central downdrafts and turbulence push the particles down to atmospheric layers where the temperature is above the condensation level, so they can sublimate and decrease the thickness of the cloud. This behavior is instead typical of cyclones.

In Figure 3 (middle row) we observe a different behavior for the stratospheric  $\text{N}_2\text{H}_4$  haze. Only Oval#3 shows a notably high column density of about  $6.0 \times 10^7$  particle/cm<sup>2</sup>. The latitudinal belt 40–35°S, which contains the three ovals, shows a diffuse and relatively thick haze (about  $4.0 \times 10^7$  particle/cm<sup>2</sup>). This haze stripe hides the presence of Oval#1 and Oval#2. These ovals cannot be identified also in the haze altitude map. Oval#3, the only one identifiable, corresponds to the minimum value of the entire map. It is characterized by increasing densities and decreasing peak altitude of the  $\text{N}_2\text{H}_4$  haze, suggesting that hydrazine is condensing at lower altitudes (around 69 km, 29 mbar). Another atmospheric structure on the east side of Oval#3 dominates the  $\text{N}_2\text{H}_4$  maps. It has both high densities ( $5.5 \times 10^7$  particle/cm<sup>2</sup>) and altitudes (71.9 km, 25.27 mbar). A possible explanation could involve an updraft centered around 63°W–38°S that, carrying tropospheric molecules to higher altitude, triggers the chemical production and condensation of hydrazine. However, this peculiar atmospheric feature will be investigated in detail in future works.

The map for the deep mixing ratio of gaseous ammonia is generally anticorrelated with the density map for the  $\text{NH}_3$ -tholin map. This suggests that, as we can expect, ammonia condenses in the deep atmosphere and then atmospheric dynamics transport the  $\text{NH}_3$  ice particles to the upper layers. While moving, they can act as condensation nuclei for hydrocarbons or other chemical products.

A peculiarity shows up in the map for the ammonia relative humidity. Oval#2 and Oval#3 show high values up to about 10.0% and 19.5%, respectively, increasing from the boundary ring toward the vortex center, whereas Oval#1 has lower values (~4–7%) with a flatter spatial distribution. This result can be explained by invoking condensation at different altitudes. Indeed, higher values for relative humidity imply lower atmospheric pressures (higher altitudes) to condense particles, and vice versa. Our finding suggests a correlation between the condensation altitude for ammonia ice particles and the relative humidity map, highlighting again the high differentiation in the dynamics of ovals in the same latitudinal belt.

An interesting atmospheric structure appears in all of our maps. It is located at latitudes slightly higher with respect to the ovals, and it has an irregular shape. It extends from 92° to 113°W longitude and from 33° to 37°S latitude (Figure 3). It is characterized by a very high column density for the  $\text{NH}_3$ -tholin cloud growing from the boundaries to the center, where it reaches values around  $1.2 \times 10^9$  particle/cm<sup>2</sup>. Consistently with the gaseous ammonia condensation at low altitude, this structure shows a very low  $\text{NH}_3$  deep mixing ratio ( $<10^{-6}$  below the saturation level). Similarly, it results to be strongly depleted in  $\text{N}_2\text{H}_4$  haze particles. Here we can sound altitudes down to about 1.3 bars, where we find the peak of the first significant cloud.

Several other atmospheric features can be recognized in our maps, whose detailed analysis is beyond the scope of this paper and will be the subject of forthcoming papers.

## 5. Conclusions

The JIRAM measurements acquired during the first orbit of Juno around Jupiter highlighted the presence of several ovals in the southern hemisphere. We selected the three ovals (Oval#1, Oval#2, and Oval#3) showing the higher contrast in the M band (around 5  $\mu\text{m}$ ) on which we performed a preliminary analysis by using the JIRAM's full spectral capability in the range of 2.4–3  $\mu\text{m}$ . This spectral range is sensitive to changes in high tropospheric clouds and in stratospheric hazes, as well as to gaseous ammonia. The application of a data

inversion algorithm based on a Bayesian approach provided information about the atmospheric structure inside and outside the oval vortices. As a result of our retrieval we produced maps of the region between 60–120°W and 30–45°S for the column densities and the altitudes of a tholin-coated NH<sub>3</sub> cloud and of an N<sub>2</sub>H<sub>4</sub> haze. Moreover, we mapped also the gaseous ammonia deep mixing ratio (below the saturation level) and its relative “humidity.”

Our results show a different behavior for the three ovals we studied. We observe evidences of a strong anticyclone producing Oval#3, where both the NH<sub>3</sub>-tholin cloud thickness and peak altitude increase toward the center. This is consistent with the central updraft that carries gaseous ammonia above the saturation level. The same structure is observed for the Oval#2 but with much less intense features. On the contrary, Oval#1, having higher cloud thickness in the boundary ring and higher cloud peak altitude in the vortex center, implies the presence of a central downdraft and thus shows evidence of a typical cyclonic structure in a giant planet. JIRAM data from further orbits will be used to monitor these behaviors.

Very high densities in the hydrazine haze with respect to other vortices and the surrounding environment also suggest the stronger activity of Oval#3. Moreover, the relative humidity map for the gaseous NH<sub>3</sub> reveals higher values in Oval#3, which implies condensation for ice particles at higher altitudes. Condensation is also observed in Oval#2 and Oval#1, though with weaker effects and at lower altitudes.

The results reported in this paper are the first obtained from JIRAM observations and therefore should be regarded as preliminary. Simultaneous analysis of solar and thermal dominated spectral range, as well as the extension to other interesting atmospheric features, could provide important insights into the clouds structure and the gaseous content in Jupiter’s atmosphere.

#### Acknowledgments

The JIRAM project is founded by the Italian Space Agency (ASI). In particular, this work has been developed under the agreement 2016-23-H.O. J.L.L. and S.K.A. acknowledge support from NASA through the Juno Project. G.S.O. acknowledges support from NASA through funds that were distributed to the Jet Propulsion Laboratory, California Institute of Technology. The JIRAM-Juno data are not currently publicly available. They will be made publicly available through the NASA Planetary Data System (<https://pds.nasa.gov>) at the end of proprietary period (currently under definition). The radiative transfer code is based on the ARS software, developed by Nikolay Ignatiev, Space Research Institute of the Russian Academy of Sciences. We thank the two anonymous reviewers, whose comments facilitated the improvement of this paper. Emiliano D’Aversa and Fabrizio Oliva (IAPS-INAF) are acknowledged for their support in software development and extensive discussion. The JIRAM instrument has been developed by Leonardo at the Officine Galileo-Campi Bisenzio site. The computational resources used in this research have been supplied by INAF-IAPS through the projects “HPP-High Performance Planetology” and “DataWell.”

#### References

- Adriani, A., et al. (2014), JIRAM, the Jovian Infrared Auroral Mapper, *Space Sci. Rev.*, doi:10.1007/s11214-014-0094-y.
- Adriani, A., M. L. Moriconi, A. Mura, F. Tosi, G. Sindoni, R. Noschese, A. Cicchetti, and G. Filacchione (2016), Juno’s Earth flyby: The Jovian Infrared Auroral Mapper preliminary results. *Astrophys. Space Sci.*, 361(8), 272, doi:10.1007/s10509-016-2842-9.
- Atreya, S. K., M. H. Wong, T. C. Owen, P. R. Mahaffy, H. B. Niemann, I. de Pater, P. Drossart, and T. Encrenaz (1999), Comparison of the atmospheres of Jupiter and Saturn: Deep atmospheric composition, cloud structure, vertical mixing, and origin, *Planet. Space Sci.*, 47, 1243–1262, doi:10.1016/S0032-0633(99)00047-1.
- Atreya, S. K., A. S. Wong, K. H. Baines, M. H. Wong, and T. C. Owen (2005), Jupiter’s ammonia clouds—Localized or ubiquitous?, *Planet. Space Sci.*, 53, 498–507.
- Baines, K. H., R. W. Carlson, and L. W. Kamp (2002), Fresh ammonia ice clouds in Jupiter. I. Spectroscopic identification, spatial distribution, and dynamical implications, *Icarus*, 159, 74–94.
- Banfield, D., P. J. Gierasch, M. Bell, E. Ustinov, A. P. Ingersoll, A. R. Vasavada, R. A. West, and M. J. S. Belton (1998), Jupiter’s cloud structure from Galileo imaging data, *Icarus*, 135, 230–250.
- Brassé, C., O. Muñoz, P. Coll, and F. Raulin (2015), Optical constants of Titan aerosols and their tholins analogs: Experimental results and modeling/observational data, *Planet. Space Sci.*, 109–110, 159–174.
- Carlson, R. W., K. H. Baines, M. S. Anderson, G. Filacchione, and A. A. Simon (2016), Chromophores from photolyzed ammonia reacting with acetylene: Application to Jupiter’s Great Red Spot, *Icarus*, 274, 106–115, doi:10.1016/j.icarus.2016.03.008.
- Clapp, M. L., and R. E. Miller (1996), Complex refractive indices of crystalline hydrazine from aerosol extinction spectra, *Icarus*, 123, 396–403.
- de Pater, I., M. H. Wong, P. Marcus, S. Luszcz-Cook, M. Ádámkóvics, A. Conrad, X. Asay-Davis, and C. Go (2010), Persistent rings in and around Jupiter’s anticyclones—Observations and theory, *Icarus*, 210, 742–762.
- de Pater, I., M. H. Wong, K. de Kleer, H. B. Hammel, M. Ádámkóvics, and A. Conrad (2011), Keck adaptive optics images of Jupiter’s north polar cap and Northern Red Oval, *Icarus*, 213, 559–563.
- Drummond, A. J., and M. P. Thekaekara (1973), *The Extraterrestrial Solar Spectrum*, Institute of Environmental Science, Mount Prospect, Ill.
- Dyudina, U. A., A. P. Ingersoll, G. E. Danielson, K. H. Baines, R. W. Carlson, and The Galileo NIMS and SSI Teams (2001), Interpretation of NIMS and SSI images on the Jovian cloud structure, *Icarus*, 150, 219–233.
- Giles, R. S., L. N. Fletcher, and P. G. J. Irwin (2015), Cloud structure and composition of Jupiter’s troposphere from 5-m Cassini VIMS spectroscopy, *Icarus*, 257, 457–470, doi:10.1016/j.icarus.2015.05.030.
- Go, C., I. de Pater, M. Wong, S. Lockwood, P. Marcus, X. Asay-Davis, and S. Shetty (2006), Evolution of the Oval BA during 2004–2005, *Bull. Am. Astron. Soc.*, 38, 495.
- Grassi, D., et al. (2010), Jupiter’s hot spots: Quantitative assessment of the retrieval capabilities of future IR spectro-imagers, *Planet. Space Sci.*, 58, 1265–1278, doi:10.1016/j.pss.2010.05.003.
- Howett, C. J. A., et al. (2007), Optical constants of ammonium hydrosulfide ice and ammonia ice, *J. Opt. Soc. Am. B*, 24(1), 126–136.
- Ignatiev, N. I., D. Grassi, and L. V. Zasova (2005), Planetary Fourier spectrometer data analysis: Fast radiative transfer models, *Planet. Space Sci.*, 53, 1035–1042, doi:10.1016/j.pss.2004.12.009.
- Irwin, P. G. J., A. L. Weir, S. E. Smith, F. W. Taylor, A. L. Lambert, S. B. Calcutt, and P. J. Cameron-Smith (1998), Cloud structure and atmospheric composition of Jupiter retrieved from Galileo near-infrared mapping spectrometer real-time spectra, *J. Geophys. Res.*, 103, 22,001–23,021, doi:10.1029/98JE00948.
- Irwin, P. G. J. (2009), *Giant Planets of Our Solar System. Atmospheres, Composition, and Structure*, 2nd ed., Springer, Praxis, Chichester, U. K.
- Kalogerakis, K. S., J. Marschall, A. U. Oza, P. A. Engel, R. T. Meharchand, and M. H. Wong (2008), The coating hypothesis for ammonia ice particles in Jupiter: Laboratory experiments and optical modeling, *Icarus*, 196, 202–215, doi:10.1016/j.icarus.2008.03.001.



- Khare, B. N., C. Sagan, E. T. Arakawa, F. Suits, T. A. Callcott, and M. W. Williams (1984), Optical constants of organic tholins produced in a simulated Titanian atmosphere: From soft X-ray to microwave frequencies, *Icarus*, *60*, 127–137.
- Moreno, F. (1996), The structure of the stratospheric aerosol layer in the equatorial and south polar regions of Jupiter, *Icarus*, *124*, 632–644.
- Peek, B. M. (1958), *The Planet Jupiter*, Faber and Faber, London.
- Quirantes, A., and A. V. Delgado (1997), The scattering of light by a suspension of coated spherical particles: Effects of polydispersity on cross sections, *J. Phys. D: Appl. Phys.*, *30*, 2123–2131.
- Rodgers, C. D. (2000), *Inverse Methods for Atmospheric Sounding: Theory and Practice*, World Sci., Singapore.
- Seiff, A., D. B. Kirk, T. C. D. Knight, R. E. Young, J. D. Mihalov, L. A. Young, F. S. Milos, G. Schubert, R. C. Blanchard, and D. Atkinson (1998), Thermal structure of Jupiter's atmosphere near the edge of a 5-m hot spot in the north equatorial belt, *J. Geophys. Res.*, *103*, 22,857–22,890, doi:10.1029/98JE01766.
- Weidenschilling, S. J., and J. S. Lewis (1973), Atmospheric and cloud structures of the Jovian planets, *Icarus*, *20*, 465–476.
- West, R. A., D. F. Strobel, and M. G. Tomasko (1986), Clouds, aerosols and photochemistry in the Jovian atmosphere, *Icarus*, *65*, 161–217.
- West, R. A., K. H. Baines, A. J. Friedson, D. Banfield, B. Ragent, and F. W. Taylor (2004), Jovian clouds and haze, in *Jupiter: The Planet, Satellites, and Magnetosphere*, edited by F. Bagenal, T. Dowling, and W. McKinnon, pp. 79–104, Cambridge Univ. Press, Cambridge.
- Youssef, A., and P. S. Marcus (2003), The dynamics of Jovian white ovals from formation to merger, *Icarus*, *162*, 74–93.